Shaping of detached image states above suspended nanowires

Dvira Segal, Petr Král, and Moshe Shapiro
Department of Chemical Physics, The Weizmann Institute of Science, Rehovot 76100, Israel
and Departments of Chemistry and Physics, The University of British Columbia, Vancouver, Canada V6T 1Z1
(Received 2 February 2004; published 14 April 2004)

We demonstrate *shaping* of image states above suspended nanowires, such as metallic nanotubes. Homogeneous infinitely long nanowires support image states *radially* detached from their surfaces, as a result of the interplay between the electrostatic attraction and centrifugal repulsion of the electron, spinning above the surface. We show that systematic introduction of inhomogeneities in the nanowire, which locally vary its screening ability, can be used to control radial detachment and *longitudinal* confinement of its image states.

DOI: 10.1103/PhysRevB.69.153405 PACS number(s): 61.46.+w, 34.60.+z, 72.20.−i, 73.22.−f

Electron image states are typically formed close to metallic surfaces,[1–3] where their lifetimes are short. In contrast, we have shown[4] that image states above suspended nanowires, such as metallic nanotubes,[5] can be highly *radially* detached from their surfaces. This unique feature of such tubular image states (TIS) is a result of the interplay between the electrostatic attraction of the external electron to the surface and the centrifugal repulsion, due to its circular motion about the cylinder's circumference. TIS for angular momenta $l \geqslant 6$ are 10–50 nm away from the surfaces. Yet the crucial problem of their confinement *along* the nanowires remains open.

In this work, we find a way of *shaping* TIS in both radial and longitudinal directions, by building inhomogeneities in the system. In Fig. 1, we see nanostructures that can fulfil this task. They are the result of joining of two or more metallic segments, such as the (12,0) and (6,6) C nanotubes. This heterojunction has a conductance gap at the Fermi energy, due to the mismatch in the rotational symmetry of the two sections.[6] Each joint thus *electrically isolates* adjacent segments by a relatively high tunneling barrier that largely blocks the flow of electric current. The barrier locally modifies the ability of the system to screen external electrons, which results in shaping of the image states above its surface.

In order to derive the electrostatic potential seen by an electron hovering above such a nanostructure, we assume that each of its segments is a perfectly conducting metallic cylinder.[4,7] Because of the radial symmetry, we can use cylindrical coordinate $\mathbf{r}=(z,\rho,\phi)$, where the electron's potential energy $V(z,\rho)$ is ϕ independent. It can be evaluated[8] from the charge distribution induced on the surface. We place a test charge q_0 at point $\mathbf{r}$ outside a *single* metallic segment and divide its surface into N tiles, with their centers residing on a grid of points $\mathbf{r}_i=(z_i,a,\phi_i)$, where a is the radius of the segment. The potential induced on the tile centered at $\mathbf{r}_i$ is given as

$$V_0(\mathbf{r}_i)=\frac{k_0 q_0}{|\mathbf{r}_i-\mathbf{r}|}+\sum_{j\neq i}\frac{k_0 q_j}{|\mathbf{r}_i-\mathbf{r}_j|}, \tag{1}$$

where $k_0=1/(4\pi\epsilon_0)$ and each q_j is the induced charge on the jth tile. Use of the charge conservation condition for the segment, $\Sigma_{i=1}^{N} q_i=0$, together with Eq. (1), and the fact that V_0 is *constant* over its entire surface, yields a set of $N+1$ linear algebraic equations for the N tile charges q_i and the surface potential V_0. Then the potential energy of the external electron at the point $\mathbf{r}$ is

$$V(\mathbf{r})=\frac{q_0}{2}\sum_{i=1}^{N}\frac{k_0 q_i}{|\mathbf{r}-\mathbf{r}_i|}, \tag{2}$$

where 1/2 eliminates double counting of the energy.

This approach can be easily extended to the case of inhomogeneous structures made up of several (isolated) segments. Then we solve the above equations for each segment, while summing over contributions from *all* the induced charges in the whole system, so as to include the segment-segment Coulombic interactions. The results of such calculations are presented in Figs. 2 and 3.

In Fig. 2, we display the induced surface-charge density for a nanotube of the length $L=200$ nm, made up of four equally long segments. For simplicity, the radius of the segments is chosen to be the same, $a=0.68$ nm, as in the (10,10) metallic nanotube, and we ignore the tube's terminal caps. We can see the accumulation of a positive screening

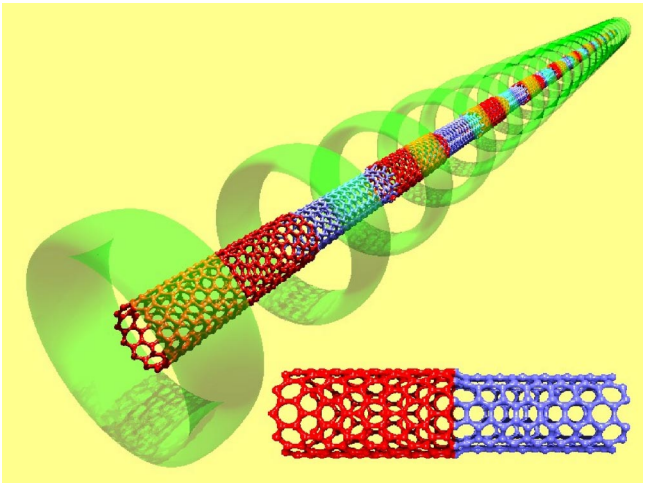

FIG. 1. (Color online) Scheme of confined ring-shaped image states, formed above joints of electrically isolated metallic segments, such as (12,0) and (6,6) metallic C nanotubes (see the inset). The states coalesce into electron image-state bands above periodic arrays of metallic segments.

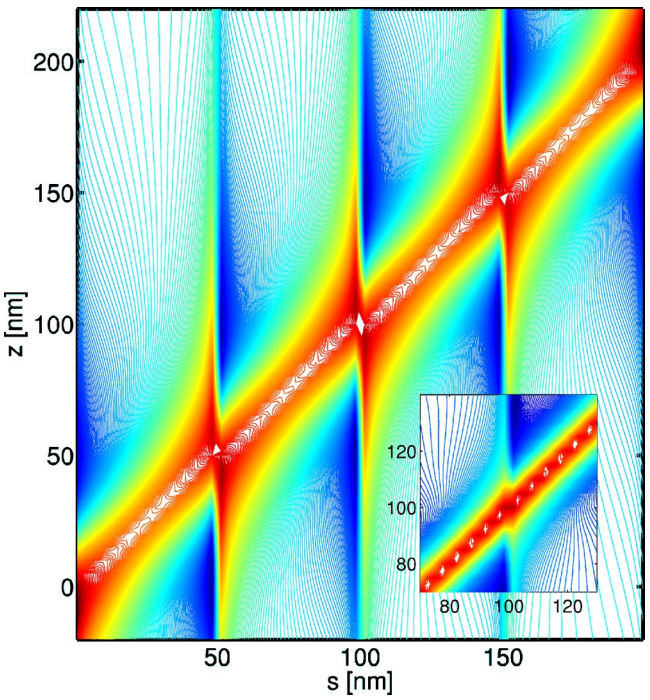

FIG. 2. (Color online) The induced charge density plotted as a function of *s*, the tube's long axis direction, and *z*, the position of the external electron along that axis. The system is made up of four 50 nm long tubular segments. The external electron is at $\rho = 30$ nm (main plot) and $\rho = 10$ nm (inset).

charge below the external electron position, extending over a tube's region comparable in size to the electron separation $\rho = 30$ (10) nm. The induced charge density is the greatest when the electron is positioned above the junctions, at $z = 50, 100$, or 150 nm. There the flow of the screening charge is the *least blocked* by the junctions. As the electron position is moved aside, dipolar double layers are formed at these junctions of the charge that is prevented to screen. This in turn makes the strongest electron attraction at the junctions.

In Fig. 3(a), we present the attractive potential energy $V(z, \rho = 10\,\text{nm})$ for an electron above a nanotube of the total length $L = 400$ nm, made up of two, four, and eight segments. We can see that the average attraction becomes *weaker* as we increase the number of segments, since the screening of the external electron is reduced. We note however that as the number of segments is multiplied by 2, the potential at the new junctions thus created remains practically the same, since no screening charge is needed to flow here. The localized quantum wells formed in the potential have the width $\Delta z \approx \rho$.

Figures 3(b,c) display the *effective* potential $V_l(z, \rho)$, including the centrifugal repulsion [see Eq. (4)]. It is calculated as a function of ρ at $z = 200$ nm for $l = 2$–6 and structures with $N = 2$ and $N = 8$ segments. For $N = 2$ and $l = 5$, the attraction gives rise to bound states, detached from the tube's surface. In the $N = 8$ case, binding is significantly reduced, so the effective potential no longer supports any detached bound states. Therefore, the existence and, in particular,

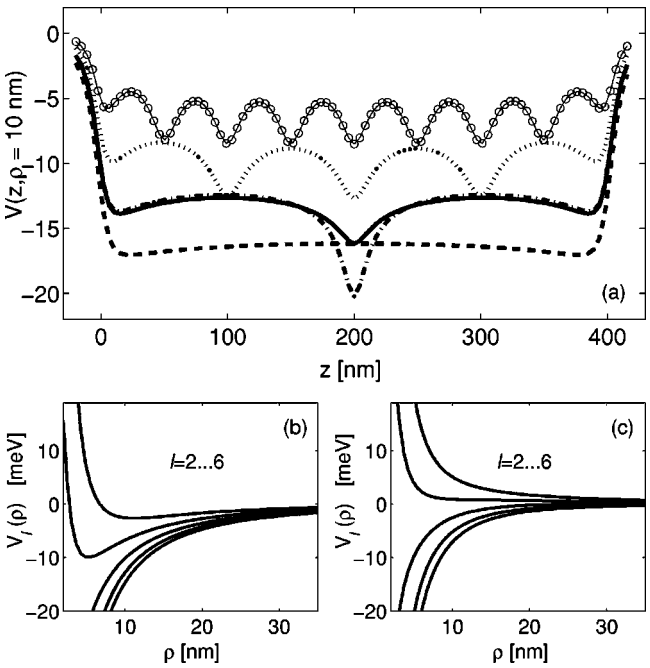

FIG. 3. (a) The induced potential energy $V(z, \rho = 10\,\text{nm})$ for (dashed line) a single segment of $L = 400$ nm; (solid line) two 200 nm segments; (dashed-dotted line) the last with no interaction of the segments; (dotted line) four 100 nm segments; and (circles) eight 50 nm segments. (b) The effective potential $V_l(z = 200\,\text{nm}, \rho)$ (including the centrifugal repulsion) for angular momenta $l = 2$–6 and system with two segments. (c) The same as in (b) for eight segments. We see that detached local minima exist in (b) but not in (c).

shaping of detached image states above nanowires could be controlled, by inserting inhomogeneities of a *different density* in the system.

We now examine these states in more detail. From the attractive potential energy $V(z, \rho)$, we can evaluate the wave functions $\Psi(z, \rho, \phi) = \psi_{l,\nu}(z, \rho)\,\Phi_l(\phi)$ of the image states, where $\Phi_l(\phi) = e^{il\phi}/\sqrt{2\pi}$, with an integer l. The radial-longitudinal part can be written in the form $\psi_{l,\nu}(z, \rho) = \chi_{l,\nu}(z, \rho)/\sqrt{\rho}$, where $\chi_{l,\nu}(z, \rho)$ is a solution of the Schrödinger equation

$$\left[\frac{-\hbar^2}{2m_e}\left(\frac{\partial^2}{\partial \rho^2} + \frac{\partial^2}{\partial z^2}\right) + V_l(z, \rho) - E_{l,\nu}\right]\chi_{l,\nu}(z, \rho) = 0. \quad (3)$$

The effective potential $V_l(z, \rho)$ combines the attractive electrostatic potential of Eq. (2) and the repulsive centrifugal potential

$$V_l(z, \rho) = V(z, \rho) + \frac{\hbar^2(l^2 - \frac{1}{4})}{2m_e\rho^2}, \quad (4)$$

where m_e is the electron mass and l is the angular momentum. We solve Eq. (3), using a multidimensional discrete variable representation (DVR) algorithm,[9] that is also used in all the other studied cases.

In Fig. 4 (lower panel), we present eigenenergies $E_{l,\nu}$ for states with $l = 5$–7, formed above a single segment of the length $L = 400$ nm [corresponding to the dashed-line poten-

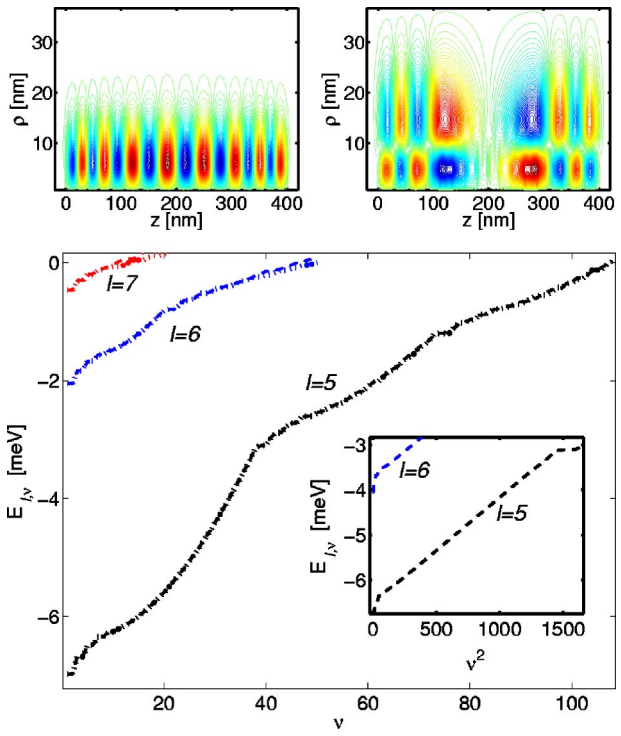

FIG. 4. (Color online) Upper panel: Two typical eigenstates, with $l=5$, of the single tube with $L=400$ nm. (a) $\nu=16$, corresponding to $(n,m)=(0,15)$ in the adiabatic approximation. (b) $\nu=48$, i.e., $(n,m)=(1,7)$. Lower panel: Comparison between the exact (dashed) and adiabatic (dotted) eigenenergies. The two sets essentially coincide. Inset: The parabolic dependence on ν of the lower-energy eigenvalues for $l=5$ and 6; the $l=6$ values are shifted by -2 meV.

tial of Fig. 3(a)]. The $l=5$ eigenstates can be grouped into several clumps, characterized by an increasing number of radial (ρ) nodes. The first clump corresponds to $\nu \lesssim 40$, where the $\nu \lesssim 10$ states are localized at the segment ends, and the second clump is at $40 \lesssim \nu \lesssim 75$. As the energy is increased in each clump, the wave functions progressively spread toward the center regions of each segment, while acquiring additional longitudinal nodes. In the inset, we show that $E_{l,\nu \lesssim 40} = C\nu^2$ for the first clump of states, where $C=2.33\times10^{-3}$ meV. This behavior is in excellent agreement with the level structure of a particle in a box of size L, for which $E_\nu = C\nu^2$, with $C=\hbar^2\pi^2/2m_eL^2=2.35\times10^{-3}$. Eigenstates with a higher number of radial nodes follow the same behavior, but this trend is masked by the intrusion of states possessing a lower number of radial nodes. Two wave functions possessing $n=0$ and $n=1$ radial node are depicted in the left and right upper panels, respectively.

These observations can be easily explained by the fact that the image-state electron moves much faster in the radial than in the longitudinal direction. We can thus apply the *adiabatic approximation*, where one solves[10] the Schrödinger equation (3) by factorizing $\chi_{l,\nu}(z,\rho)$ as

$$\chi_{l,\nu}(z,\rho) = \varphi_n^l(z,\rho)\, G_{n,m}^l(z). \tag{5}$$

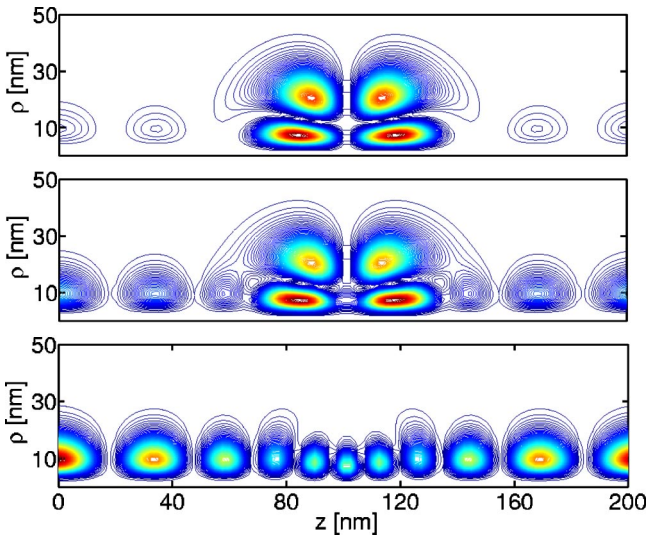

FIG. 5. (Color online) Probability density for states in the 12th band, presented for (top) $kL=0$, (middle) $kL=2.3$, (bottom) $kL=\pi$. The change in localization and symmetry of the wave functions is caused by hybridization of different types of states.

Here, $\varphi_n^l(z,\rho)$ are solutions of the one-dimensional *radial* equation in ρ, with z as a parameter,

$$\left(\frac{-\hbar^2}{2m_e}\frac{\partial^2}{\partial\rho^2} + V_l(z,\rho)\right)\varphi_n^l(z,\rho) = \epsilon_n^l(z)\varphi_n^l(z,\rho). \tag{6}$$

The adiabatic eigenvalues $\epsilon_n^l(z)$, obtained from Eq. (6), are then used as the potentials for the *longitudinal* eigenvalue equation for $G_{n,m}^l(z)$,

$$\left(\frac{-\hbar^2}{2m_e}\frac{\partial^2}{\partial z^2} + \epsilon_n^l(z)\right) G_{n,m}^l(z) = E_{n,m}^l\, G_{n,m}^l(z). \tag{7}$$

This approximation greatly reduces the calculation effort, because instead of solving the two-dimensional Schrödinger equation [Eq. (3)], it involves solving just two one-dimensional problems. We can thus assign every ν level two adiabatic quantum numbers n and m, which measure the number of radial and longitudinal nodes, respectively. As demonstrated in Fig. 4 (lower panel), the adiabatic eigenenergies obtained from Eqs. (5)–(7) deviate by less than 1% from the exact eigenvalues for the presented angular momenta l.

Let us now proceed to the case, shown in Fig. 1, of infinitely long, periodic linear arrays of isolated metallic segments. The attractive potential for this system is $V(z+R,\rho)=V(z,\rho)$, where $R=jL$, with j being an integer and L signifying the lattice constant. Thus the wave functions of the system are the Bloch states

$$\chi_{\nu,k}^l(z,\rho) = e^{ikz} f_{\nu,k}^l(z,\rho) = e^{ikz} f_{\nu,k}^l(z+R,\rho), \tag{8}$$

with band index ν, quasimomentum $\hbar k$, and angular momentum $\hbar l$. The functions $f_{\nu,k}^l$ fulfill the equation

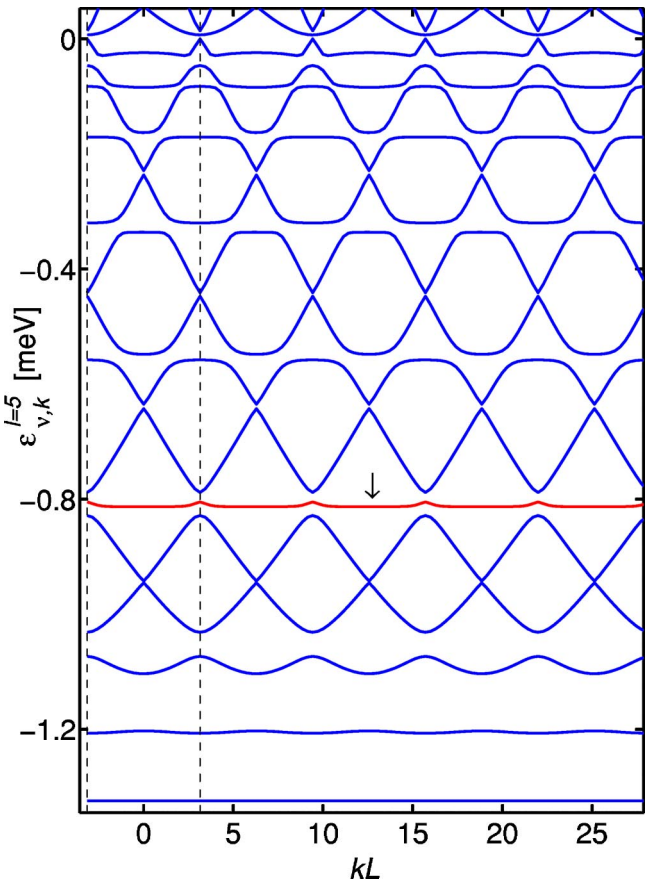

FIG. 6. (Color online) Band structure of image states with $l=5$ above an array of $L=200$ nm nanotube segments. Displayed are the $\nu=7-25$ bands, with the flat 12th band marked in both the reduced (vertical dashed lines) and extended zones.

$$\left\{\frac{-\hbar^2}{2m_e}\left[\frac{\partial^2}{\partial\rho^2}+\left(\frac{d}{dz}+ik\right)^2\right]+V_l(z,\rho)\right\}f^l_{\nu,k}(z,\rho)$$
$$=\epsilon^l_{\nu,k}\,f^l_{\nu,k}(z,\rho), \tag{9}$$

which can be solved numerically, using the DVR algorithm.[9] We have also confirmed here the excellent validity of the adiabatic approximation, given by equations analogous to Eqs. (5)–(7).

In Fig. 5 we display the probability densities for three $l=5$ states of a periodic system of metallic segments, with the lattice constant $L=200$ nm. They belong to $k=0, 2.3/L, \pi/L$ in the 12th band (see Fig. 6). We can clearly see that the excitation changes from being radial to being longitudinal, due to *hybridization* of states of different localizations and symmetries. Therefore, features found in finite systems are naturally incorporated into image states above periodically modulated nanowires.

In Fig. 6, we present band energies $\epsilon^{l=5}_{\nu,k}$. The lowest bands are almost flat, since they correspond to states highly localized above junctions between neighboring segments. Many of the higher bands can be smoothly connected in the extended zone into one nearly parabolic band. States belonging to these bands have an increasing number of longitudinal nodes, but they possess no radial nodes. These steeply varying bands are hybridized with some flat bands (e.g., the 12th band) of states with additional radial nodes and fewer longitudinal nodes.

These effects should be observable also in *disordered* nanowires, with a reduced screening ability. In particular, the *average* attractive potential and image-state wave functions above a periodic system with L long segments could be similar to those above a disordered nanowire with the *localization length* L. This fact might serve as a measure of conduction-electron localization. We can even devise a *genetic algorithm*, which for a chosen profile of the attractive potential would find an optimal profile of inhomogeneities or disorder in the system.

Note that *detached* TIS can be also prepared above thicker circularly symmetric metallic nanostructures. We can find that, for a tube of radius $a \ll L$, the eigenenergies roughly behave like $E_{l,\nu} \propto 1/a$, while detached wave functions, typically observable for angular momenta $l \propto \sqrt{a}$, are separated $\approx 10a$ from the tube. For $a=40$ nm detached states with $l \approx 50$ are formed 400 nm away from the surface. By shaping image states above such nanostructures, we can control the motion of electrons and molecules, including proteins,[11] around them.

We acknowledge H. R. Sadeghpour and B. E. Granger for numerous discussions. This project was supported by the German-Israeli Foundation, the EU IHP program Contract No. HPRN-CT-1999-00129, and the Office of Naval Research.

[1] N.D. Lang and W. Kohn, Phys. Rev. B **7**, 3541 (1973).
[2] P.M. Echenique, F. Flores, and F. Sols, Phys. Rev. Lett. **55**, 2348 (1985).
[3] U. Höfer, I.L. Shumay, Ch. Reuß, U. Thomann, W. Wallauer, and Th. Fauster, Science **277**, 1480 (1997).
[4] B.E. Granger, P. Král, H.R. Sadeghpour, and M. Shapiro, Phys. Rev. Lett. **89**, 135506 (2002).
[5] M.S. Dresselhaus, G. Dresselhaus, and Ph. Avouris, *Carbon Nanotubes: Synthesis, Structure, Properties and Applications* (Springer-Verlag, Berlin, 2001).
[6] L. Chico, L.X. Benedict, S.G. Louie, and M.L. Cohen, Phys. Rev. B **54**, 2600 (1996).
[7] J.D. Jackson, *Classical Electrodynamics*, 2nd ed. (Wiley, New York, 1975).
[8] P. Keblinski, S.K. Nayak, P. Zapol, and P.M. Ajayan, Phys. Rev. Lett. **89**, 255503 (2002).
[9] S. Kanfer and M. Shapiro, J. Phys. Chem. **88**, 3964 (1984); D.T. Colbert and W.H. Miller, J. Chem. Phys. **96**, 1982 (1992); J.C. Light and T. Carrington, Adv. Chem. Phys. **114**, 263 (2000).
[10] M. Shapiro and M.S. Child, J. Chem. Phys. **76**, 6176 (1982).
[11] P. Král, Chem. Phys. Lett. **382**, 399 (2003).